ACS Catalysis

pubs.acs.org/acscatalysis Research Article

Manipulating Coordination Structures of Mixed-Valence Copper Single Atoms on 1T-MoS_2 for Efficient Hydrogen Evolution

Zhida Li,[▽] Xingxu Yan,[▽] Dong He,[▽] Wenhui Hu, Sabrina Younan, Zunjian Ke, Margaret Patrick, Xiangheng Xiao, Jier Huang, Hongjun Wu,* Xiaoqing Pan,* and Jing Gu*

Cite This: *ACS Catal.* 2022, 12, 7687−7695 Read Online

ACCESS | Metrics & More | Article Recommendations | Supporting Information

ABSTRACT: Directing single atoms (SAs) to occupy specific lattice sites in support materials and correlating the resulting changes in atomic coordination structures to catalytic activity are crucial for the rational design of high-performance single-atom catalysts (SACs). Herein, for the same copper (Cu) SAs, two coordination structures on 1T-phase molybdenum disulfide (MoS_2) are identified. In the adsorption model, Cu SAs are coordinated onto the outermost sulfur (S) plane in a trigonal pyramidal geometry (Cu_{ads}@MoS_2), while in the substitution model, Cu SAs are substituted with molybdenum (Mo) atoms (Cu_{sub}@MoS_2), octahedrally coordinating with six S atoms in 1T-MoS_2. Interestingly, in both coordination models, Cu(I) and Cu(II) SAs simultaneously exist. Cu_{ads}@MoS_2 (173 mV) and Cu_{sub}@MoS_2 (160 mV) demonstrate significantly reduced overpotential (at 10 mA cm^{-2}) for the hydrogen evolution reaction (HER) compared to that of 1T-MoS_2 (235 mV) under acidic condition (0.5 M H_2SO_4). Additionally, theoretical results reveal that different coordination structures would result in distinct active sites, where in Cu_{ads}@MoS_2, the Cu SAs are the active sites, whereas in Cu_{sub}@MoS_2, the S atoms most adjacent to the Cu SAs are the major active sites. Accurately determining the atomic coordination structures of SAs and uncovering their structure−property relationships are essential to guiding future geometry and structural research on SACs.

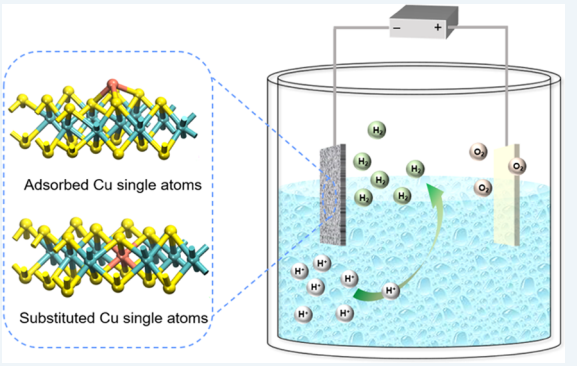

KEYWORDS: *1T-MoS_2, copper single atom, coordination structures, hydrogen evolution reaction, active sites*

1. INTRODUCTION

The ever-increasing atmospheric carbon dioxide (CO_2) levels, derived from the immoderate consumption of fossil fuels, are forcing society to search for sustainable alternatives to coal, petroleum, and natural gas. Compared to carbon-based fuels, hydrogen (H_2) is considered an ideal candidate as the only byproduct of its use is water.[1] Unfortunately, H_2 is mainly produced from highly centralized, energy- and carbon-extensive steam reformation and partial oxidation of coal and other hydrocarbons.[2] By comparison, renewable energy-powered electrochemical water splitting provides the most promising alternative to traditional, energetically demanding industrial processes due to the advantages of decentralization, reduced energy input, and low carbon footprint.

Noble metals, such as platinum (Pt), are well recognized as top-performing hydrogen evolution reaction (HER) electrocatalysts.[3,4] However, the high cost and scarcity of Pt hinder its large-scale application. Significant advances have been made to develop promising low-cost alternatives.[5] For instance, MoS_2 has attracted tremendous interest as an inexpensive replacement for precious-metal-based electrocatalysts.[6−10] Unfortunately, the catalytic activity of MoS_2 is vastly inferior to that of Pt, which is mainly attributed to its limited active sites.[6−10] In the semiconducting 2H phase of MoS_2 (2H-MoS_2), active sites are located at the coordinatively unsaturated S atoms along its edges, leaving large numbers of basal plane S atoms inert.[11] In contrast, the metallic 1T phase (1T-MoS_2) exhibits enlarged interlayer spacing, which exposes active sites along the basal plane in addition to the edges.[12,13] Consequently, 1T-MoS_2 possesses exceptional electronic conductivity and superior HER activity.[14] One major drawback to 1T-MoS_2 is the metastability it suffers from, which limits its catalytic performance.[15] Fortunately, it may be stabilized by doping transition metals with valence electrons capable of completing the occupation of the low-lying t_{2g} orbitals of 1T-MoS_2.[14]

Similar to transition-metal dopants, single atoms (SAs) disperse throughout supports by forming chemical bonds and transferring electrons to the Mo t_{2g} orbitals.[16] The incorporation of SAs provides an opportunity to further enhance HER

Received: February 11, 2022
Revised: June 1, 2022
Published: June 14, 2022

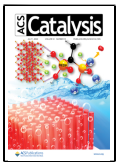

https://doi.org/10.1021/acscatal.2c00759
ACS Catal. 2022, 12, 7687−7695

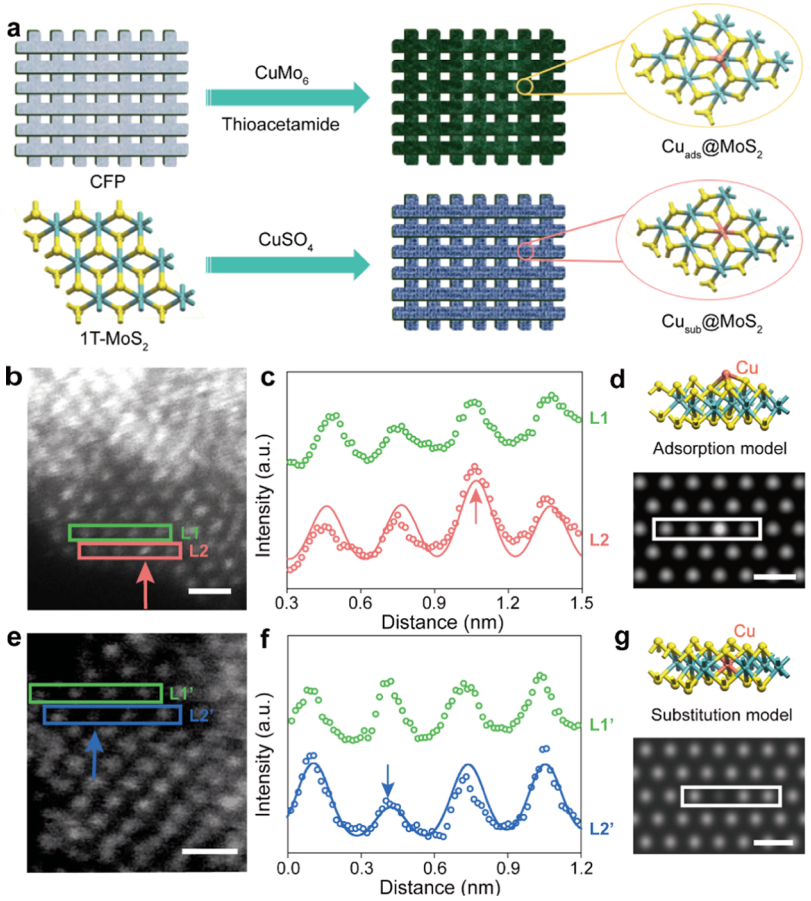

Figure 1. Synthetic strategies and STEM characterization of Cu SA-modified 1T-MoS_2. (a) Synthesis illustration of Cu SA-modified 1T-MoS_2. HAADF-STEM analysis of (b–d) Cu_{ads}@MoS_2 and (e–g) Cu_{sub}@MoS_2. (b) Atomic-resolution HAADF image of Cu_{ads}@MoS_2 with a scale bar of 0.5 nm. (c) Intensity profiles taken along two adjacent lines (L1 and L2) in (b). (d) Side-view atomic structures and simulated HAADF image of Cu_{ads}@MoS_2 with a scale bar of 0.5 nm; (e–g) belong to Cu_{sub}@MoS_2 and follow a similar sequence. In intensity profiles (c and f), open circles represent the experimental data taken along L1 and L2 (L1′ and L2′) and solid lines represent the simulated data. In structural diagrams (d and g, top), yellow, cyan, and red balls are S, Mo, and Cu atoms, respectively.

activity and stabilize 1T-MoS_2.[17−19] For instance, our group reported the synthesis of 1T-MoS_2 with atomically dispersed nickel (Ni) SAs (NiO@1T-MoS_2), which exhibited an overpotential of only 46 mV at the current density of 10 mA cm^{-2} in alkaline electrolyte.[17] In another example, Ji et al.[18] designed a one-pot solvothermal method to synthesize 1T-MoS_2 integrated with Cu SAs, which required an overpotential of 131 mV (10 mA cm^{-2}) and displayed a visible decrease in overpotential compared to 1T-MoS_2 (~250 mV). These works demonstrate the feasibility of enhancing the electrocatalytic performance of 1T-MoS_2 by introducing SAs either as active sites or facilitators to escalate MoS_2's activity.

In homogeneous catalysts, the atomic coordination structures dictate their catalytic activity.[20] Akin to homogeneous catalysts, understanding the atomic coordination structures of SAs is critically important to understand the catalytic activity of single-atom catalysts (SACs). However, most SACs produced from pyrolysis contain various coordination structures.[20] Furthermore, it is difficult to accurately identify coordination structures in general on three-dimensional (3D) supports. On the contrary, benefiting from their well-defined layered atomic structure and exposed basal planes, two-dimensional (2D) supports such as MoS_2 provide the characteristics necessary for quantitative identification of the anchoring sites and coordination environments of SACs.

Herein, two types of 1T-MoS_2 and copper (Cu) SA coordination structures were studied, which we refer to as the substitution and adsorption models. In the substitution model, Cu SAs substitute Mo atoms (Cu_{sub}@MoS_2), while in the adsorption model, Cu SAs adsorb atop S atoms on the basal plane (Cu_{ads}@MoS_2). To date, hardly any research is able to precisely distinguish those two models with the same SA, along with their coordination geometries and influences on the electronic states and catalytic activities. Their atomic structures were carefully identified by advanced microscopy and verified by X-ray absorption spectroscopy. Further, the atomic coordination structures were correlated closely with their active sites and catalytic activity. This work paves a rational pathway toward designing SA-modified 2D materials and provides an in-depth understanding of the structure-induced activity differences in 2D materials modified with SAs.

2. RESULTS AND DISCUSSION

2.1. Advanced Microscopy Characterization and Identification of SA Coordination Structures. In this work, Cu_{ads}@MoS_2 was obtained using the one-pot hydrothermal method, converting from an Anderson-type polyoxometalate (POM) precursor ($(NH_4)_4[CuH_6Mo_6O_{24}]\cdot xH_2O$,

https://doi.org/10.1021/acscatal.2c00759
ACS Catal. 2022, 12, 7687−7695

denoted by $CuMo_6$), while $Cu_{sub}@MoS_2$ was synthesized via an implantation strategy in which presynthesized 1T-MoS_2 was reacted with $CuSO_4{\cdot}5H_2O$ (Figure 1a). As reported previously, the oxidation of Mo in MoS_2 leads to the formation of Mo vacancies, while the reduction of Mo creates S vacancies.[13] XPS characterization of $Cu_{sub}@MoS_2$ (Figure S1 and Table S1) supports the coexistence of Mo^{4+}, Mo^{5+}, and Mo^{6+}, where high-valence Mo is possibly derived from the oxidation of the lower-valence Mo, creating Mo vacant sites. When reacting with $CuSO_4{\cdot}5H_2O$, Cu^{2+} tends to occupy the Mo vacant site and form stable Cu−S bonds. By comparison, the direct conversion of $CuMo_6$ and thioacetamide leads to the formation of $Cu_{ads}@MoS_2$. This phenomenon might be explained by the fact that the $CuMo_6$ precursor mixed with thioacetamide and ammonium molybdate (para) tetrahydrate was subjected to hydrothermal recrystallization where bonding cleavage and reformation occur ($Cu_{ads}@MoS_2$). In this way, two different types of Cu SAs confined in 1T-MoS_2 were achieved.

To demonstrate the dispersity of SAs, energy-dispersive X-ray spectroscopy (EDS) mapping was employed. In the EDS mapping, $Cu_{ads}@MoS_2$ and $Cu_{sub}@MoS_2$ demonstrate the uniform distribution of Cu, Mo, S, and oxygen (O) (Figures S3 and S4). Further, the locations of Cu SAs on 1T-MoS_2 were precisely identified by high-angle annular dark-field (HAADF) scanning transmission electron microscopy (STEM). In a HAADF-STEM image, elements with higher atomic numbers produce brighter signal intensities than those with lower atomic numbers due to the nature of *Z*-contrast sensitivity.[21] In Figure 1b, the brighter dot (distinguished by the red arrow in L2) identifies a Cu SA positioned right above a Mo atom, confirming the formation of $Cu_{ads}@MoS_2$. Further support for this result is provided by the intensity profiles (Figure 1c), where the visibly higher ADF intensity of the third atom in L2 verifies that the Cu SA adsorbed onto the outmost layer of S, atop a Mo atom. Simulated structural diagrams and STEM imaging further verify the coordination structure of $Cu_{ads}@MoS_2$ (Figure 1d), in agreement with experimental results. Contrastingly, the darker spot shown in Figure 1e illustrates the substitution of a Mo atom by a Cu SA ($Cu_{sub}@MoS_2$), which is further supported by the intensity profiles (Figure 1f). Similarly, the simulated structural diagram and STEM image of $Cu_{sub}@MoS_2$ (Figure 1g) match nicely with the experimental results. To exclude this as a local phenomenon, HAADF images were collected across various regions of $Cu_{ads}@MoS_2$ and $Cu_{sub}@MoS_2$ (Figure S5). Even with the highest Cu dosage, Cu still presents as SAs in both adsorption and substitution samples (Figures S6 and S7). The STEM results demonstrate the successful synthesis of two Cu SA coordination models.

2.2. Structural Characterization and Electronic Structures. The structural differences between the two distinct coordination structure models ($Cu_{ads}@MoS_2$ and $Cu_{sub}@MoS_2$) were further revealed by Raman spectroscopy (Figure S8 and Table S2). For all samples analyzed, the low-frequency Raman peaks around 147, 219, and 283 cm^{-1} corresponding to the J_1, J_2, and J_3 phonon modes, along with the E_{1g} mode at 335 cm^{-1} confirm the phase of MoS_2 to be 1T.[13,22,23] Vibrational modes around 375 and 400 cm^{-1} are assigned to the $E_{2g}{}^1$ and A_{1g} phonon modes, respectively.[24−26] Here, the $E_{2g}{}^1$ mode represents the opposing in-plane vibrations of S atoms relative to Mo atoms, while A_{1g} illustrates an out-of-plane lattice expansion.[27,28] Upon forming bonding interactions with Cu SAs, both $E_{2g}{}^1$ and A_{1g} modes exhibit an observable blueshift compared to that of 1T-MoS_2. Raman signals of $E_{2g}{}^1$ and A_{1g} reveal the thickness and number of layers, where the blueshift indicates an interlayer and in-plane alternation of 1T-MoS_2 induced by the incorporation of Cu SAs.[25,29]

In both samples, X-ray diffraction (XRD) patterns produced characteristic 2θ diffraction peaks at 14, 32, and 35°, which correspond to the (002), (100), and (102) planes of MoS_2 (Figure S9a). The broad shoulder along the (002) plane confirms the extremely thin nanosheet features, while the much stronger and sharper peak along (002) confirms the presence of stacked hexagonal MoS_2 layers (Figure S9b).[30] Furthermore, X-ray photoelectron spectroscopy (XPS) was employed to characterize the surface chemistry of 1T-MoS_2, $Cu_{ads}@MoS_2$, and $Cu_{sub}@MoS_2$ (Figures S1 and S2, and Table S1). In all samples, the doublet peaks centered at around 162.3 and 163.9 eV were assigned to S $2p_{3/2}$ and S $2p_{1/2}$, respectively.[31,32] The S^{6+} peak present around 169.6 eV is assigned to physically adsorbed sulfate ions.[17] The second set of doublet peaks arising in the S 2p region is associated with the presence of amorphous MoS_x. The Mo 3d doublet peaks centered around 229.4 and 232.6 eV are assigned to Mo^{4+},[33] 230.1 and 233.5 eV are assigned to MoS_x (Mo^{5+}), while the peak present at around 236.1 eV is ascribed to Mo^{6+}, likely caused by the partial oxidation of surficial Mo^{4+} and Mo^{5+}.[34] Cu $2p_{3/2}$ spectra located at around 932.7 ($Cu_{ads}@MoS_2$) and 933.9 eV ($Cu_{sub}@MoS_2$) confirm the presence of Cu SAs and support the conclusion that the chemical structures of the two Cu SAs are different.[18] From the comparison of the S 2p region, a negative shift in S $2p_{3/2}$ and S $2p_{1/2}$ was observed for $Cu_{ads}@MoS_2$ (161.7 and 163.3 eV) and $Cu_{sub}@MoS_2$ (161.9 and 163.7 eV) relative to 1T-MoS_2 (162.3 and 163.9 eV). This shift suggests that the introduction of Cu SAs facilitates the electron transfer from Cu SAs to S atoms.[17] Herein, XPS shows the influence of incorporating Cu SAs into 1T-MoS_2 and distinguishable structural differences between the two models of $Cu@MoS_2$.

Further changes in the electronic structures of $Cu_{ads}@MoS_2$ and $Cu_{sub}@MoS_2$ were disclosed by electron paramagnetic resonance (EPR) spectra (Figure S10 and Table S3). Herein, 2H-MoS_2 and 1T-MoS_2 are employed as control samples, which show significant differences. 2H-MoS_2 displays a relatively narrow and strong signal of characteristic g value at 2.005, which is attributed to the existence of S-coordinated defects.[35] By comparison, 1T-MoS_2 presents four different signals located at g values of 2.042, 2.012, 1.976, and 1.936 respectively. The resonance at g = 2.012 is assigned to the same S-coordinated defects as in 2H-MoS_2. After incorporating Cu SAs into 1T-MoS_2, the EPR signal intensities decrease with respect to pristine 1T-MoS_2, indicating a reduction in S-coordinated defects possibly due to the coordination of defected S atoms to the Cu SAs. The corresponding peaks shift slightly along 1T-MoS_2, $Cu_{ads}@MoS_2$, and $Cu_{sub}@MoS_2$, which is likely caused by slight structural differences between those samples.[36] $Cu_{ads}@MoS_2$ and $Cu_{sub}@MoS_2$ demonstrated distinct changes in g values (Table S3), suggesting that different coordination structures exist for $Cu_{ads}@MoS_2$ and $Cu_{sub}@MoS_2$, consistent with the STEM results (Figure 1). All 1T-MoS_2 samples show an EPR signal with a g factor ranging from 2.040 to 2.045 (denoted by signal 1 in Figure S10), which may be assigned to the presence of paramagnetic S atoms.[36] The weak signal with a g factor of 1.965 to 1.980 is assigned to the $Mo^{\delta+}$ oxygenated species in MoS_x.[35] Overall, the EPR

https://doi.org/10.1021/acscatal.2c00759
ACS Catal. 2022, 12, 7687−7695

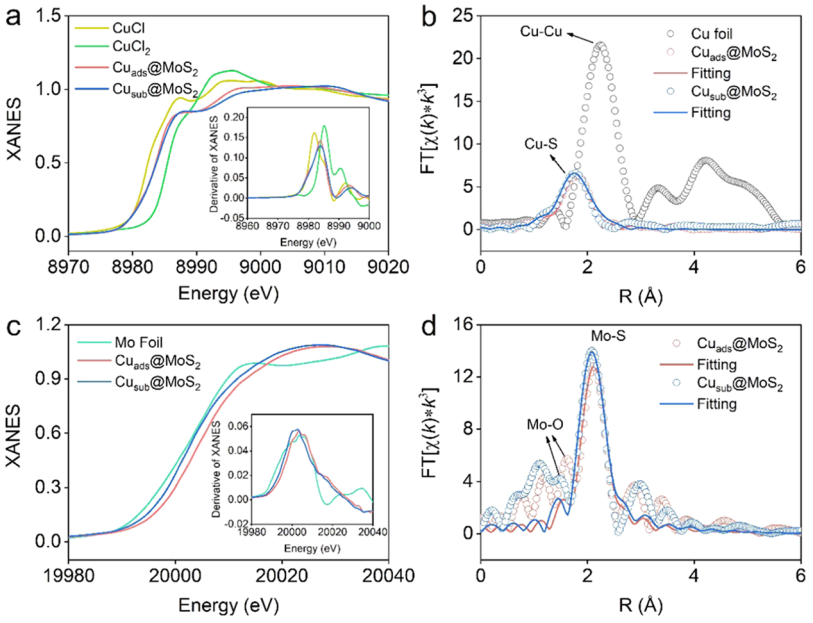

Figure 2. X-ray absorption analysis of $Cu_{ads}@MoS_2$ and $Cu_{sub}@MoS_2$ at the Cu K-edge (a, b) and Mo K-edge (c, d). (a, c) Normalized XANES spectra. (b, d) Fourier transforms of EXAFS spectra in R-space (open circles) and best-fitting lines (solid lines). The insets in (a, c) are the first derivative of the corresponding XANES spectra.

spectra provide solid evidence of the structural differences between 2H-MoS_2, 1T-MoS_2, $Cu_{ads}@MoS_2$, and $Cu_{sub}@MoS_2$.

2.3. Local Geometry and Coordination Environment. X-ray absorption spectroscopy (XAS) was used to examine the local environment at both Cu and Mo centers (Figure 2) in $Cu_{ads}@MoS_2$ and $Cu_{sub}@MoS_2$. The X-ray absorption near edge structure (XANES) spectra of both $Cu_{ads}@MoS_2$ and $Cu_{sub}@MoS_2$ at Cu K-edge show the absorption edges between Cu(I)Cl and Cu(II)Cl_2 (Figure 2a), suggesting that Cu SAs in $Cu_{ads}@MoS_2$ and $Cu_{sub}@MoS_2$ have a unique valence state located between +1 and +2. The extended X-ray absorption fine structure (EXAFS) spectra in the R-space of both samples (Figure 2b) only show the presence of Cu−S bonding (~1.8 Å) without Cu−Cu bonding (2.2 Å), supporting that the Cu atoms in $Cu_{ads}@MoS_2$ and $Cu_{sub}@MoS_2$ exist as SAs rather than Cu clusters.[18,37−39] Additionally, the EXAFS spectra (Figures 2b and S11) simulated based on the adsorption and substitution structures modeled by density functional theory (DFT) calculation correspond well with the experimental data, where the fitting results support that there is only one type of Cu−S bond in $Cu_{ads}@MoS_2$ (Cu coordinates to three S atoms) but two types of Cu−S bonds in $Cu_{sub}@MoS_2$ (the axial and equatorial Cu−S bonds in the octahedral structure with lengths equal to 2.710 and 2.236 Å, respectively) (Table S4). These results confirm the Cu SAs' distinct atomic coordination structures between $Cu_{ads}@MoS_2$ and $Cu_{sub}@MoS_2$.

Figure 2c shows the XANES spectra of Mo foil, $Cu_{ads}@MoS_2$, and $Cu_{sub}@MoS_2$ at Mo K-edge corresponding to the 1s−5p transition.[17] A visible difference is identified between $Cu_{ads}@MoS_2$ and $Cu_{sub}@MoS_2$ in the absorption edge position, indicating the existence of different local coordination environments surrounding the Mo center induced by different Cu SA anchoring sites. The Fourier transforms of Mo K-edge EXAFS spectra in K-space (Figure S12) and *R*-space (Figure 2d) indicate different anchoring sites cause a little change in Mo-S bond length, as evidenced by the slight shift of $Cu_{ads}@MoS_2$ to longer bond length compared to $Cu_{sub}@MoS_2$. Furthermore, the longer the Mo−S bond length, the weaker the Mo−S bond strength, which is consistent with the Gibbs free energy of 2.030 eV ($Cu_{ads}@MoS_2$) and 2.052 eV ($Cu_{sub}@MoS_2$) (Table S5). The presence of Mo−O bonds is also verified (marked by arrows, Figure 2d). This verification is based on a previous study that recognizes the bond length differences between Mo−S (1.9 Å) and Mo−O (1.2 Å).[40] The structural parameters around Mo atoms were obtained and are demonstrated in Table S5. Together, XAS results prove the different coordination environments surrounding Cu and Mo centers in $Cu_{ads}@MoS_2$ and $Cu_{sub}@MoS_2$.

To learn more about the intervalence of Cu, electron energy loss spectroscopy (EELS) with the capability to distinguish local Cu oxidation states was performed. Previously, Wang and co-workers employed EELS to identify the nuances between CuO, Cu_2O, and mixed-valence Cu_3O_4, where the mixed-valence Cu_3O_4 demonstrates a stronger peak with an energy loss of ~930 eV corresponding to Cu^{2+} and a weaker peak at ~933 eV for Cu^{1+}.[41] Nassiri et al. found similar trends, where the energy positions of the Cu L edge negatively shifted for higher oxidation states.[42] This is also the case for this work (Figure S13 and Table S6). The intervalence of Cu SAs in $Cu_{ads}@MoS_2$ and $Cu_{sub}@MoS_2$ was caused by the coexistence of Cu(I) and Cu (II). As clearly shown in Figure S13c and S13d, the Cu L3 edge in $Cu_{ads}@MoS_2$ exhibits two resolved peaks with respective energy losses of 930.0 and 935.3 eV. The resolved peaks at the Cu L2 edge with respective energy losses of 952.8 and 957.5 eV match with the L3 edge, providing supporting evidence for the coexistence of both valence states. Similarly, in $Cu_{sub}@MoS_2$ (Figure S13g and S13h), Cu(II) and Cu(I) species, with respective energy losses of 929.1 and 935.8 eV at Cu L3 edge, together with Cu L2 edge with respective energy losses of 950.7 and 957.9 eV, confirm the coexistence of Cu(I) and Cu(II). Here, EELS features help us unravel the unique mixed-valence states of Cu SAs.

https://doi.org/10.1021/acscatal.2c00759
ACS Catal. 2022, 12, 7687−7695

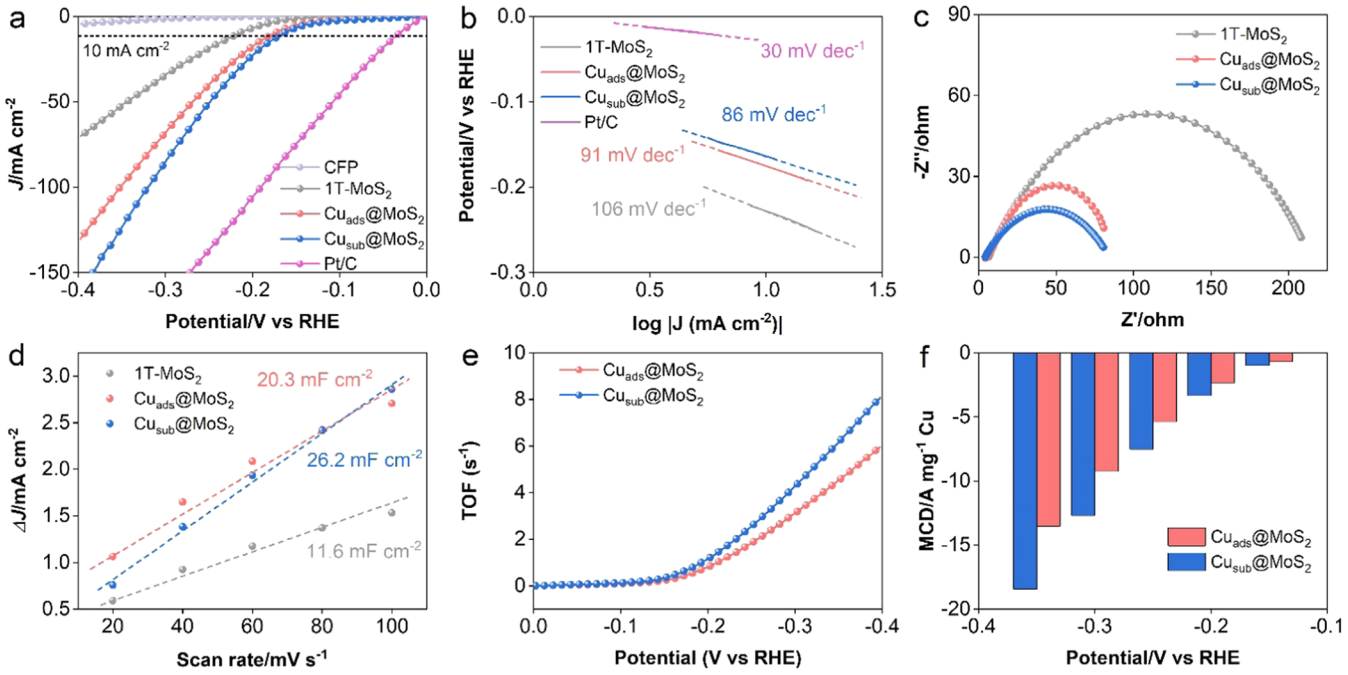

Figure 3. Electrochemical characterization of the 1T-MoS_2 modified by Cu SAs in 0.5 M H_2SO_4 in a three-electrode configuration. (a) Polarization curves of the HER for CFP, 1T-MoS_2, Cu_{ads}@MoS_2, Cu_{sub}@MoS_2, and Pt/C. (b) Tafel plots of 1T-MoS_2, Cu_{ads}@MoS_2, Cu_{sub}@MoS_2, and Pt/C. (c) Fitted EIS spectra of 1T-MoS_2, Cu_{ads}@MoS_2, and Cu_{sub}@MoS_2 measured at the potential of −150 mV vs RHE (see the equivalent circuit model in Figure S16). (d) Scan rate dependence of current density. (e) TOF values of Cu_{ads}@MoS_2 and Cu_{sub}@MoS_2. (f) MCD of the catalysts on the basis of Cu.

2.4. Catalytic Activity Measurement. Electrochemical measurements were carried out within a standard three-electrode electrochemical cell configuration in 0.5 M H_2SO_4 saturated with N_2 (Figure 3). First, we evaluated the loading amounts of Cu on 1T-MoS_2, as shown in Table S7, and corresponding polarization curves are shown in Figure S14. Along with the increasing dosage of Cu precursor ($CuMo_6$), Cu loading amounts in Cu_{ads}@MoS_2 gradually increase from 0.12% of 0.5 mg $CuMo_6$ (the corresponding sample is denoted by 0.5 Cu_{ads}@MoS_2) to 0.32% of 2.0 Cu_{ads}@MoS_2, 0.72% of 2.5 Cu_{ads}@MoS_2, and finally to 1.12% of 4.0 Cu_{ads}@MoS_2 (Table S7). Moreover, with increasing weight percent of Cu, the overpotential at 10 mA cm^{-2} decreases from 194 mV at 0.12% Cu to 181 mV at 0.32% Cu, and to a minimum 173 mV at 0.72% Cu, then increases to 197 mV at a higher Cu loading of 1.12% (Figure S14a). Cu_{sub}@MoS_2 samples exhibit similar trends in both Cu loading and catalytic performance. As the Cu precursor ($CuSO_4$ solution) increases, Cu loading in Cu_{sub}@MoS_2 presents an increase from 0.15% of 0.2 mL of $CuSO_4$ solution (the corresponding sample is denoted by 0.2 Cu_{sub}@MoS_2) to 0.26% of 0.5 Cu_{sub}@MoS_2, 0.66% of 1.5 Cu_{sub}@MoS_2, and finally to 1.08% of 2.0 Cu_{sub}@MoS_2 (Table S7). Polarization curves shown in Figure S14b suggest that the overpotential required by Cu_{sub}@MoS_2 to generate 10 mA cm^{-2} decreases from 207 mV of 0.2 Cu_{sub}@MoS_2 to 182 mV of 0.5 Cu_{sub}@MoS_2, to the optimal 160 mV of 1.5 Cu_{sub}@MoS_2, and then increases to 187 mV of 2.0 Cu_{sub}@MoS_2. These results signify that a proper concentration of Cu SAs with an appropriate inter-SA distance might influence the electronic structure of SAs, which is essential to tune a catalyst's activity.[43] For simplification, in the following context, the optimal 2.5 Cu_{ads}@MoS_2 and 1.5 Cu_{sub}@MoS_2 were denoted by Cu_{ads}@MoS_2 and Cu_{sub}@MoS_2 in this work to compare with controlled 1T-MoS_2 and Pt/C. As shown by the polarization curves in Figure 3a, Cu_{ads}@MoS_2 and Cu_{sub}@MoS_2 both show greater HER performance relative to 1T-MoS_2, as the overpotential (at 10 mA cm^{-2}) decreases from 235 mV (1T-MoS_2) to 173 mV (Cu_{ads}@MoS_2) and 160 mV (Cu_{sub}@MoS_2), respectively. To obtain more insight into the HER kinetics, Tafel slopes were evaluated (Figures 3b and S15). Under acidic conditions, the hydrogen adsorption step proceeds via the Volmer reaction, in which a proton captures an electron at the electrode surface to form the adsorbed hydrogen atom ($H^+ + e^- \rightarrow H_{ads}$).[5,44,45] Afterward, H_2 formation occurs through one of the two following pathways: the Heyrovsky reaction ($H_{ads} + H^+ + e^- \rightarrow H_2$) or the Tafel reaction ($H_{ads} + H_{ads} \rightarrow H_2$). In the Heyrovsky pathway (low H_{ads} coverage case), one electron and one proton are transferred to the H_{ads}, resulting in the desorption and generation of H_2, while in the Tafel mechanism (high H_{ads} coverage case), two H_{ads}'s are combined on the electrode surface to generate H_2. These two pathways both involve the adsorption and desorption of H_{ads}. Based on Sabatier principles, the interactions between the catalyst and substrate should be "just right" to result in optimal HER performance.[46] Herein, the large Tafel slope produced by 1T-MoS_2 (106 mV dec^{-1}) indicates that 1T-MoS_2 follows the Volmer−Heyrovsky mechanism, where the Volmer step is the rate-determining step.[47] For Cu_{ads}@MoS_2 and Cu_{sub}@MoS_2, the Tafel slope visibly reduces to 91 and 86 mV dec^{-1}, respectively. This result suggests that Cu SAs in both models enhance the HER kinetics of 1T-MoS_2 but still follow the Volmer−Heyrovsky mechanism.

Furthermore, the aforementioned conclusions were supported by electrochemical impedance spectroscopy (EIS) (Figures 3c and S16 and Table S9). Compared to 1T-MoS_2

https://doi.org/10.1021/acscatal.2c00759
ACS Catal. 2022, 12, 7687−7695

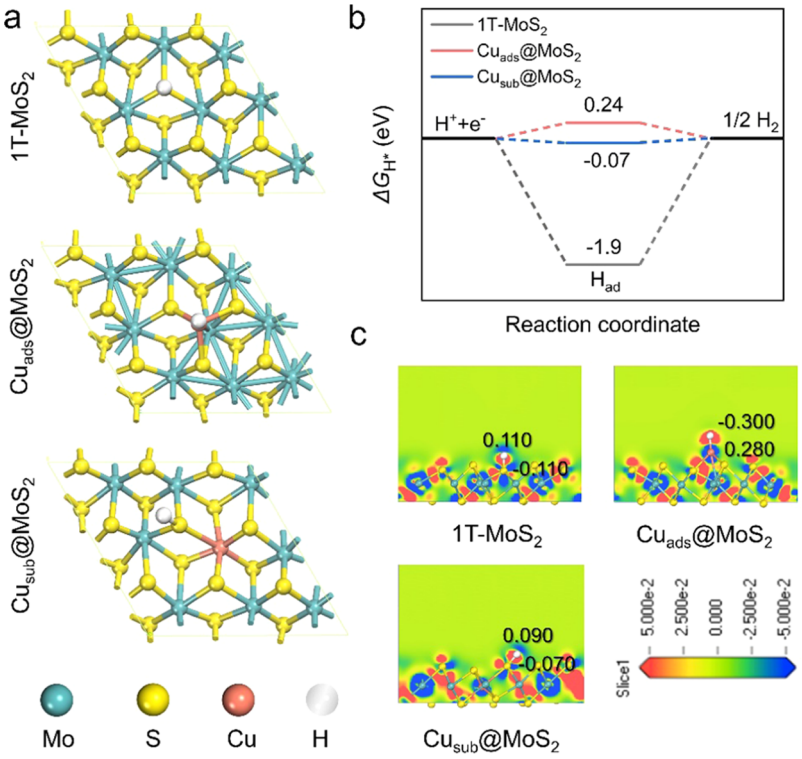

Figure 4. Computational results of 1T-MoS_2 decorated by Cu SAs for the HER. (a) Hydrogen adsorption modes on 1T-MoS_2, Cu_{ads}@MoS_2, and Cu_{sub}@MoS_2. (b) Calculated ΔG_{H^*} for the HER at a potential of 0 V vs RHE at pH = 0 for 1T-MoS_2, Cu_{ads}@MoS_2, and Cu_{sub}@MoS_2. (c) Electron density differences of hydrogen adsorption on 1T-MoS_2, Cu_{ads}@MoS_2, and Cu_{sub}@MoS_2, respectively. The red and blue regions can be indexed by Slice 1 (electron density differences before and after H* adsorption).

(207.4 Ω), the charge transfer resistance (R_{ct}) values of Cu_{ads}@MoS_2 (103.0 Ω) and Cu_{sub}@MoS_2 (80.1 Ω) are considerably lower, signifying a visible enhancement in charge transfer and HER kinetics. The equivalent series resistance (R_s) of 1T-MoS_2, Cu_{ads}@MoS_2, and Cu_{sub}@MoS_2 falls in the range of 4−6 Ω, which is unsurprising since all working electrodes were following the same preparation procedures and measured in the same solution. The electrochemical double-layer capacitances (C_{dl}) were measured by cyclic voltammetry (CV) (Figure S17) to derive the active surface area (Figure 3d). Herein, Cu_{ads}@MoS_2 and Cu_{sub}@MoS_2 exhibit C_{dl} values nearly 2 times higher (20.3 and 26.2 mF cm^{-2}, respectively) than that of 1T-MoS_2 (11.6 mF cm^{-2}), demonstrating the enhancement of active sites in 1T-MoS_2 after Cu SA modification. These results confirm that Cu SAs, whether adsorbed or substituted, enhance the electrocatalytic activity of 1T-MoS_2. Turnover frequency (TOF) values of Cu_{ads}@MoS_2 and Cu_{sub}@MoS_2 were calculated and are displayed in Figure 3e. Similar to the polarization curves, the TOF values increase with higher potential, similar to previous work.[18] Furthermore, the TOF values of Cu_{ads}@MoS_2 and Cu_{sub}@MoS_2 at a 400 mV overpotential were quantified to be 6.12 and 8.27 s^{-1}, respectively, on the basis of ICP-OES results (Table S7), suggesting Cu_{sub}@MoS_2 has a higher HER activity than Cu_{ads}@MoS_2. To further compare the intrinsic activities of Cu in different SA models, mass activities were measured by calculating the mass current density (MCD) based on the Cu loading amounts (Table S7), as shown in Figure 3f. The MCD of Cu_{sub}@MoS_2 is higher than that of Cu_{ads}@MoS_2 under the same potential, as exemplified by −18.4 and −13.5 A per mg Cu at −0.35 V vs RHE in Cu_{sub}@MoS_2 and Cu_{ads}@MoS_2, respectively. All results suggest that Cu in Cu_{sub}@MoS_2 should be more active than in Cu_{ads}@MoS_2. To evaluate the durability of these two catalysts, we compared their polarization curves before and after running CV scans for 1000 cycles (Figure S18). A negligible negative shift (less than 10 mV at the current density of 10 mA cm^{-2}) was observed after 1000 cycles for both Cu_{ads}@MoS_2 and Cu_{sub}@MoS_2, thus confirming satisfied stabilities of both Cu_{ads}@MoS_2 and Cu_{sub}@MoS_2. The XPS characterization on postelectrolysis Cu_{ads}@MoS_2 and Cu_{sub}@MoS_2 revealed that the MoS_2 substrate underwent slightly chemical oxidation during the HER process (Figure S1). However, it does not influence the HER performance visibly due to the unchanged LSV in the preelectrolysis and postelectrolysis samples (Figure S18). Structural reorganization during catalysis is very common for MoS_2 and has been extensively reported in the literature.[48−50] HAADF-STEM and EELS results of postelectrolysis Cu_{ads}@MoS_2 and Cu_{sub}@MoS_2 implied that Cu showed atomic dispersion with intervalence feature (Figures S19 and S20). Overall, the HER activities of Cu_{ads}@MoS_2 and Cu_{sub}@MoS_2 are comparable to state-of-the-art SA-modified MoS_2 catalysts (Table S10). SAs such as Zn,[51] Ni,[52] Cu,[18] and Pt[11] exhibit similar overpotentials (130, 110, 131, and 145 mV, respectively) when anchored on MoS_2.

2.5. Density Functional Theory Calculations. The underlying mechanism of the enhanced HER performance induced by the Cu SAs was further disclosed by first-principles DFT calculations. The constructed slab models for DFT calculations are shown in Figure S21. H* adsorptions on 1T-MoS_2, Cu_{ads}@MoS_2, and Cu_{sub}@MoS_2 are shown in Figure 4a. First, the electronic structure was calculated to reveal the role of Cu SAs. Compared with 1T-MoS_2, the Hirshfeld charges of the S atoms adjacent to the Cu SAs in Cu_{sub}@MoS_2 become more negative, which suggests that electrons are transferred

https://doi.org/10.1021/acscatal.2c00759
ACS Catal. 2022, 12, 7687−7695

from the Cu SAs to the surrounding S atoms (Figure S22). This observation correlates well with the XPS results (Table S1), where the binding energies in the S 2p spectra shift negatively when introducing Cu SAs (~0.5 eV). This indicates that Cu SAs can effectively change the electronic structures of the original S active sites in 1T-MoS_2.

Second, the optimal active states for adsorbed hydrogen (H*) and their related Gibbs free energy diagram (ΔG_{H^*}) were calculated (Figure 4b). Here, the large ΔG_{H^*} calculated for 1T-MoS_2 (−1.9 eV) indicates that H* adsorbs strongly to the S active sites, which will inhibit the desorption of H*. As expected, the incorporation of Cu SAs dramatically increases ΔG_{H^*} from −1.9 eV (1T-MoS_2) to 0.24 eV (Cu_{ads}@MoS_2) and −0.07 eV (Cu_{sub}@MoS_2), facilitating the H* desorption process. The catalytic performance of Cu-modified 1T-MoS_2 exhibits more competent thermodynamics compared to 1T-MoS_2. The electronic structure changes upon adsorbing H* on 1T-MoS_2, Cu_{ads}@MoS_2, and Cu_{sub}@MoS_2 were then examined to gain further insights into the catalytic mechanism of Cu SAs on the HER (Figure 4c). For 1T-MoS_2, H* directly bonds to the S sites, acting as an electron donor and exhibiting a positive valence state. This is also the case for Cu_{sub}@MoS_2, where H* adsorbs on the S atoms that are adjacent to Cu. For Cu_{ads}@MoS_2, since H* adsorbs on the Cu atom, it functions as an electron acceptor and exhibits a negative valence state. Therefore, the incorporation of Cu SAs will induce the weakened adsorption of the H* on the surface of catalysts, and H* transforms from an electron donor to an electron acceptor in Cu_{ads}@MoS_2. This would greatly promote the desorption of H* and account for the near-zero ΔG_{H^*}. From the above discussion, we can further confirm that in Cu_{ads}@MoS_2, the Cu SAs themselves act as the main active sites while the S atoms adjacent to the Cu SAs in Cu_{sub}@MoS_2 are the main active sites. The ability to differentiate the coordination structures of SAs on the substrate and correlate the structural differences with variations in catalytic mechanisms is critical for the future development of cutting-edge catalysts.

3. CONCLUSIONS

In summary, two types of Cu SAs supported by 1T-MoS_2 were identified and prepared: Cu_{ads}@MoS_2 and Cu_{sub}@MoS_2. The HAADF-STEM results provide solid evidence of the adsorption and substitution models in Cu_{ads}@MoS_2 and Cu_{sub}@MoS_2, respectively, while XAS further confirms the bonding structures. Overpotentials at 10 mA cm^{-2} exhibited by Cu_{ads}@MoS_2 (173 mV) and Cu_{sub}@MoS_2 (160 mV) demonstrate their enhanced HER performance compared to 1T-MoS_2 (235 mV) under acidic condition (0.5 M H_2SO_4). DFT calculations indicate that the Cu SAs facilitate the desorption of H* by regulating the electronic structure of 1T-MoS_2 and increasing ΔG_{H^*} from −1.9 eV (1T-MoS_2) to 0.24 eV (Cu_{ads}@MoS_2) and −0.07 eV (Cu_{sub}@MoS_2). Furthermore, DFT predictions indicate that with the same SAs, their function in HER catalysis is completely different. In Cu_{ads}@MoS_2, Cu acts as an active site, while only acting as a facilitator, which promotes the activity of adjacent S atoms in Cu_{sub}@MoS_2. As SAs are stabilized by bonding interaction with supports, the ability to manipulate the coordination structures of SAs will enable the fine-control of SAC activity and selectivity. By providing an insightful understanding of the lattice sites occupied by SAs and the resulting impact on catalytic activity, this work is expected to pave the way for the design and development of high-performing SACs.

ASSOCIATED CONTENT

Supporting Information

The Supporting Information is available free of charge at https://pubs.acs.org/doi/10.1021/acscatal.2c00759.

Experimental details, EDS mappings, HAADF-STEM images, Raman spectra, XRD, XPS spectra, EPR spectra, EELS spectra, electrochemical data, and DFT models (PDF)

AUTHOR INFORMATION

Corresponding Authors

Hongjun Wu − *Department of Chemistry and Biochemistry, San Diego State University, San Diego, California 92182-1030, United States; College of Chemistry & Chemical Engineering, Northeast Petroleum University, Daqing 163318, China*; Email: hjwu@nepu.edu.cn

Xiaoqing Pan − *Department of Materials Science and Engineering, University of California, Irvine, California 92697, United States; Department of Physics and Astronomy, University of California, Irvine, California 92697, United States*; Email: xiaoqing.pan@uci.edu

Jing Gu − *Department of Chemistry and Biochemistry, San Diego State University, San Diego, California 92182-1030, United States*; orcid.org/0000-0002-5506-0049; Email: jgu@sdsu.edu

Authors

Zhida Li − *Department of Chemistry and Biochemistry, San Diego State University, San Diego, California 92182-1030, United States; College of Chemistry & Chemical Engineering, Northeast Petroleum University, Daqing 163318, China*

Xingxu Yan − *Department of Materials Science and Engineering, University of California, Irvine, California 92697, United States*; orcid.org/0000-0001-7991-4849

Dong He − *Department of Physics and Key Laboratory of Artificial Micro- and Nanostructures of Ministry of Education; Institute of Technological Sciences, Wuhan University, Wuhan 430072, China*

Wenhui Hu − *Department of Chemistry, Marquette University, Milwaukee, Wisconsin 53201, United States*

Sabrina Younan − *Department of Chemistry and Biochemistry, San Diego State University, San Diego, California 92182-1030, United States*

Zunjian Ke − *Department of Chemistry and Biochemistry, San Diego State University, San Diego, California 92182-1030, United States; Department of Physics and Key Laboratory of Artificial Micro- and Nanostructures of Ministry of Education; Institute of Technological Sciences, Wuhan University, Wuhan 430072, China*

Margaret Patrick − *Department of Chemistry and Biochemistry, San Diego State University, San Diego, California 92182-1030, United States*

Xiangheng Xiao − *Department of Physics and Key Laboratory of Artificial Micro- and Nanostructures of Ministry of Education; Institute of Technological Sciences, Wuhan University, Wuhan 430072, China*; orcid.org/0000-0001-9111-1619

Jier Huang − *Department of Chemistry, Marquette University, Milwaukee, Wisconsin 53201, United States*; orcid.org/0000-0002-2885-5786

Complete contact information is available at: https://pubs.acs.org/10.1021/acscatal.2c00759

https://doi.org/10.1021/acscatal.2c00759
ACS Catal. 2022, 12, 7687−7695

Author Contributions

[▽]Z.L., X.Y., and D.H. contributed equally to this work. The manuscript was written through contributions of all authors. All authors have given approval to the final version of the manuscript.

Notes

The authors declare no competing financial interest.

■ ACKNOWLEDGMENTS

J.G. acknowledges San Diego State University (SDSU) start-up funds and NSF award (CEBT-1704992) to support this research. The work at University of California, Irvine, was supported by the NSF through grants CBET-2031494 and CHE- 1955786. The authors acknowledge the use of facilities and instrumentation at the Irvine Materials Research Institute supported in part by NSF through the University of California Irvine Materials Research Science and Engineering Center (DMR-2011967) and the Major Research Instrumentation Program (CHE-1338173). H.W. thanks the financial support from the National Natural Science Foundation of China (NSFC no. 21476046), Science Fund for Distinguished Young Scholars of Heilongjiang Province of China (no. JC2017002), and Special Fund of Northeast Petroleum University (no. GLJHB201901). The numerical calculations in this paper have been done on the supercomputing system in the Supercomputing Center of University of Science and Technology of China. Use of the Advanced Photon Source in Argonne National Laboratory was supported by the U. S. Department of Energy, Office of Science, Office of Basic Energy Sciences, under Award No. DE-AC02−06CH11357.

■ REFERENCES

(1) Niaz, S.; Manzoor, T.; Pandith, A. H. Hydrogen storage: Materials, methods and perspectives. *Renewable Sustainable Energy Rev.* **2015**, *50*, 457−469.
(2) Kothari, R.; Buddhi, D.; Sawhney, R. Comparison of environmental and economic aspects of various hydrogen production methods. *Renewable Sustainable Energy Rev.* **2008**, *12*, 553−563.
(3) Li, C.; Baek, J.-B. Recent Advances in Noble Metal (Pt, Ru, and Ir)-Based Electrocatalysts for Efficient Hydrogen Evolution Reaction. *ACS Omega* **2020**, *5*, 31−40.
(4) Liu, T.; Gao, W.; Wang, Q.; Dou, M.; Zhang, Z.; Wang, F. Selective Loading of Atomic Platinum on a RuCeOx Support Enables Stable Hydrogen Evolution at High Current Densities. *Angew. Chem., Int. Ed.* **2020**, *59*, 20423−20427.
(5) Zou, X.; Zhang, Y. Noble metal-free hydrogen evolution catalysts for water splitting. *Chem. Soc. Rev.* **2015**, *44*, 5148−5180.
(6) Shi, S.; Gao, D.; Xia, B.; Liu, P.; Xue, D. Enhanced hydrogen evolution catalysis in MoS_2 nanosheets by incorporation of a metal phase. *J. Mater. Chem. A* **2015**, *3*, 24414−24421.
(7) Tsai, C.; Abild-Pedersen, F.; Nørskov, J. K. Tuning the MoS_2 edge-site activity for hydrogen evolution via support interactions. *Nano Lett.* **2014**, *14*, 1381−1387.
(8) Shi, Y.; Wang, J.; Wang, C.; Zhai, T.-T.; Bao, W.-J.; Xu, J.-J.; Xia, X.-H.; Chen, H.-Y. Hot electron of Au nanorods activates the electrocatalysis of hydrogen evolution on MoS_2 nanosheets. *J. Am. Chem. Soc.* **2015**, *137*, 7365−7370.
(9) Jaramillo, T. F.; Jørgensen, K. P.; Bonde, J.; Nielsen, J. H.; et al. Sebastian Horch, Ib Chorkendorff, Identification of Active Edge Sites for Electrochemical H_2 Evolution from MoS_2 Nanocatalysts. *Science* **2007**, *317*, 100−102.
(10) Yu, Y.; Huang, S.-Y.; Li, Y.; Steinmann, S. N.; Yang, W.; Cao, L. Layer-dependent electrocatalysis of MoS_2 for hydrogen evolution. *Nano Lett.* **2014**, *14*, 553−558.
(11) Deng, J.; Li, H.; Xiao, J.; Tu, Y.; Deng, D.; Yang, H.; Tian, H.; Li, J.; Ren, P.; Bao, X. Triggering the electrocatalytic hydrogen evolution activity of the inert two-dimensional MoS_2 surface via single-atom metal doping. *Energy Environ. Sci.* **2015**, *8*, 1594−1601.
(12) Acerce, M.; Voiry, D.; Chhowalla, M. Metallic 1T phase MoS_2 nanosheets as supercapacitor electrode materials. *Nat. Nanotechnol.* **2015**, *10*, 313−318.
(13) Luo, Z.; Ouyang, Y.; Zhang, H.; Xiao, M.; Ge, J.; Jiang, Z.; Wang, J.; Tang, D.; Cao, X.; Liu, C.; Xing, W. Chemically activating MoS_2 via spontaneous atomic palladium interfacial doping towards efficient hydrogen evolution. *Nat. Commun.* **2018**, *9*, No. 2120.
(14) Lei, Z.; Zhan, J.; Tang, L.; Zhang, Y.; Wang, Y. Recent Development of Metallic (1T) Phase of Molybdenum Disulfide for Energy Conversion and Storage. *Adv. Energy Mater.* **2018**, *8*, No. 1703482.
(15) Jayabal, S.; Wu, J.; Chen, J.; Geng, D.; Meng, X. Metallic 1T-MoS_2 nanosheets and their composite materials: Preparation, properties and emerging applications. *Mater. Today Energy* **2018**, *10*, 264−279.
(16) Yang, X.-F.; Wang, A.; Qiao, B.; Li, J.; Liu, J.; Zhang, T. Single-Atom Catalysts: A New Frontier in Heterogeneous Catalysis. *Acc. Chem. Res.* **2013**, *46*, 1740−1748.
(17) Huang, Y.; Sun, Y.; Zheng, X.; Aoki, T.; Pattengale, B.; Huang, J.; He, X.; Bian, W.; Younan, S.; Williams, N.; et al. Atomically engineering activation sites onto metallic 1T-MoS_2 catalysts for enhanced electrochemical hydrogen evolution. *Nat. Commun.* **2019**, *10*, No. 982.
(18) Ji, L.; Yan, P.; Zhu, C.; Ma, C.; Wu, W.; Wei, C.; Shen, Y.; Chu, S.; Wang, J.; Du, Y.; et al. One-pot synthesis of porous 1T-phase MoS_2 integrated with single-atom Cu doping for enhancing electrocatalytic hydrogen evolution reaction. *Appl. Catal., B* **2019**, *251*, 87−93.
(19) Qiao, W.; Xu, W.; Xu, X.; Wu, L.; Yan, S.; Wang, D. Construction of Active Orbital via Single-Atom Cobalt Anchoring on the Surface of 1T-MoS_2 Basal Plane toward Efficient Hydrogen Evolution. *ACS Appl. Energy Mater.* **2020**, *3*, 2315−2322.
(20) Lu, B.; Liu, Q.; Chen, S. Electrocatalysis of Single-Atom Sites: Impacts of Atomic Coordination. *ACS Catal.* **2020**, *10*, 7584−7618.
(21) Crewe, A. V.; Wall, J.; Langmore, J. Visibility of single atoms. *Science* **1970**, *168*, 1338−1340.
(22) Zhang, J.; Xu, X.; Yang, L.; Cheng, D.; Cao, D. Single-Atom Ru Doping Induced Phase Transition of MoS_2 and S Vacancy for Hydrogen Evolution Reaction. *Small Methods* **2019**, *3*, No. 1900653.
(23) Er, E.; Hou, H.-L.; Criado, A.; Langer, J.; Möller, M.; Erk, N.; Liz-Marzán, L. M.; Prato, M. High-Yield Preparation of Exfoliated 1T-MoS_2 with SERS Activity. *Chem. Mater.* **2019**, *31*, 5725−5734.
(24) Wilson, J. A.; Yoffe, A. D. The transition metal dichalcogenides discussion and interpretation of the observed optical, electrical and structural properties. *Adv. Phys.* **1969**, *18*, 193−335.
(25) Li, H.; Zhang, Q.; Yap, C. C. R.; Tay, B. K.; Edwin, T. H. T.; Olivier, A.; Baillargeat, D. From Bulk to Monolayer MoS_2: Evolution of Raman Scattering. *Adv. Funct. Mater.* **2012**, *22*, 1385−1390.
(26) Late, D. J.; Liu, B.; Matte, H. R.; Rao, C.; Dravid, V. P. Rapid characterization of ultrathin layers of chalcogenides on SiO_2/Si substrates. *Adv. Funct. Mater.* **2012**, *22*, 1894−1905.
(27) Bertrand, P. A. Surface-phonon dispersion of MoS_2. *Phys. Rev. B* **1991**, *44*, 5745.
(28) Zhou, K.-G.; Withers, F.; Cao, Y.; Hu, S.; Yu, G.; Casiraghi, C. Raman modes of MoS_2 used as fingerprint of van der Waals interactions in 2-D crystal-based heterostructures. *ACS Nano* **2014**, *8*, 9914−9924.
(29) Lee, C.; Yan, H.; Brus, L. E.; Heinz, T. F.; Hone, J.; Ryu, S. Anomalous lattice vibrations of single-and few-layer MoS_2. *ACS Nano* **2010**, *4*, 2695−2700.
(30) Li, Y.; Wang, L.; Zhang, S.; Dong, X.; Song, Y.; Cai, T.; Liu, Y. Cracked monolayer 1T MoS_2 with abundant active sites for enhanced electrocatalytic hydrogen evolution. *Catal. Sci. Technol.* **2017**, *7*, 718−724.

https://doi.org/10.1021/acscatal.2c00759
ACS Catal. 2022, 12, 7687−7695

(31) Wu, Y.; Li, F.; Chen, W.; Xiang, Q.; Ma, Y.; Zhu, H.; Tao, P.; Song, C.; Shang, W.; Deng, T.; Wu, J. Coupling interface constructions of $MoS_2/Fe_5Ni_4S_8$ heterostructures for efficient electrochemical water splitting. *Adv. Mater.* **2018**, *30*, No. 1803151.
(32) Yin, Y.; Han, J.; Zhang, Y.; Zhang, X.; Xu, P.; Yuan, Q.; Samad, L.; Wang, X.; Wang, Y.; Zhang, Z.; et al. Contributions of phase, sulfur vacancies, and edges to the hydrogen evolution reaction catalytic activity of porous molybdenum disulfide nanosheets. *J. Am. Chem. Soc.* **2016**, *138*, 7965−7972.
(33) Anjum, M. A. R.; Jeong, H. Y.; Lee, M. H.; Shin, H. S.; Lee, J. S. Efficient Hydrogen Evolution Reaction Catalysis in Alkaline Media by All-in-One MoS_2 with Multifunctional Active Sites. *Adv. Mater.* **2018**, *30*, No. 1707105.
(34) Ye, R.; del Angel-Vicente, P.; Vicente, D. P. D. A.; Liu, D. Y.; Arellano-Jimenez, D. J.; Peng, D. Z.; Wang, T.; Li, Y.; Yakobson, P. D. B. I.; Wei, D. S.-H.; Yacaman, P. D. M. J. High-performance hydrogen evolution from $MoS_{2(1-x)}P_x$ solid solution. *Adv. Mater.* **2016**, *28*, 1427−1432.
(35) Panich, A. M.; Shames, A. I.; Rosentsveig, R.; Tenne, R. A magnetic resonance study of MoS_2 fullerene-like nanoparticles. *J. Phys. Condens. Matter* **2009**, *21*, No. 395301.
(36) González, J. R.; Alcántara, R.; Tirado, J. L.; Fielding, A. J.; Dryfe, R. A. W. Electrochemical Interaction of Few-Layer Molybdenum Disulfide Composites vs Sodium: New Insights on the Reaction Mechanism. *Chem. Mater.* **2017**, *29*, 5886−5895.
(37) Nayak, C.; Bhattacharyya, D.; Jha, S. N.; Sahoo, N. K. In Situ XAS Study on Growth of PVP-Stabilized Cu Nanoparticles. *ChemistrySelect* **2018**, *3*, 7370−7377.
(38) Han, G.; Zheng, Y.; Zhang, X.; Wang, Z.; Sun, X.; et al. High loading single-atom Cu dispersed on graphene for efficient oxygen reduction reaction. *Nano Energy* **2019**, *66*, No. 104088.
(39) Li, F.; Han, G.-F.; Noh, H.-J.; Kim, S.-J.; Lu, Y.; Jeong, H. Y.; Fu, Z.; Baek, J.-B. Boosting oxygen reduction catalysis with abundant copper single atom active sites. *Energy Environ. Sci.* **2018**, *11*, 2263−2269.
(40) Tang, C.; Jiao, Y.; Shi, B.; Liu, J.-N.; Xie, Z.; Chen, X.; Zhang, Q.; Qiao, S.-Z. Coordination Tunes Selectivity: Two-Electron Oxygen Reduction on High-Loading Molybdenum Single-Atom Catalysts. *Angew. Chem., Int. Ed.* **2020**, *59*, 9171−9176.
(41) Wang, Y.; Lany, S.; Ghanbaja, J.; Fagot-Revurat, Y.; Chen, Y. P.; Soldera, F.; Horwat, D.; Mücklich, F.; Pierson, J. F. Electronic structures of Cu_2O, Cu_4O_3, and CuO: A joint experimental and theoretical study. *Phys. Rev. B* **2016**, *94*, No. 245418.
(42) Nassiri, Y.; Mansot, J. L.; Wéry, J.; Ginsburger-Vogel, T.; Amiard, J. C. Ultrastructural and Electron Energy Loss Spectroscopy Studies of Sequestration Mechanisms of Cd and Cu in the Marine Diatom Skeletonema costatum. *Arch. Environ. Contam. Toxicol.* **1997**, *33*, 147−155.
(43) Meng, X.; Ma, C.; Jiang, L.; Si, R.; Meng, X.; Tu, Y.; Yu, L.; Bao, X.; Deng, D. Distance Synergy of MoS_2-Confined Rhodium Atoms for Highly Efficient Hydrogen Evolution. *Angew. Chem., Int. Ed.* **2020**, *59*, 10502−10507.
(44) Shi, Y.; Zhang, B. Recent advances in transition metal phosphide nanomaterials: synthesis and applications in hydrogen evolution reaction. *Chem. Soc. Rev.* **2016**, *45*, 1529−1541.
(45) Li, Y.; Wang, H.; Xie, L.; Liang, Y.; Hong, G.; Dai, H. MoS_2 nanoparticles grown on graphene: an advanced catalyst for the hydrogen evolution reaction. *J. Am. Chem. Soc.* **2011**, *133*, 7296−7299.
(46) Cheng, J.; Hu, P. Utilization of the three-dimensional volcano surface to understand the chemistry of multiphase systems in heterogeneous catalysis. *J. Am. Chem. Soc.* **2008**, *130*, 10868.
(47) Tang, Q.; Jiang, D. E. Mechanism of Hydrogen Evolution Reaction on 1T-MoS_2 from First Principles. *ACS Catal.* **2016**, *6*, 4953−4961.
(48) Mu, X.; Zhu, Y.; Gu, X.; Dai, S.; Mao, Q.; Bao, L.; Li, W.; Liu, S.; Bao, J.; Mu, S. Awakening the oxygen evolution activity of MoS_2 by oxophilic-metal induced surface reorganization engineering. *J. Energy Chem.* **2021**, *62*, 546−551.
(49) Ahn, E.; Kim, B.-S. Multidimensional Thin Film Hybrid Electrodes with MoS_2 Multilayer for Electrocatalytic Hydrogen Evolution Reaction. *ACS Appl. Mater. Interfaces* **2017**, *9*, 8688−8695.
(50) Feng, J.; Zhao, Z.; Tang, R.; Zhao, Y.; Meng, T. Interfacial Structural and Electronic Regulation of MoS_2 for Promoting Its Kinetics and Activity of Alkaline Hydrogen Evolution. *ACS Appl. Mater. Interfaces* **2021**, *13*, 53262−53270.
(51) Shi, Y.; Zhou, Y.; Yang, D.-R.; Xu, W.-X.; Wang, C.; Wang, F.-B.; Xu, J.-J.; Xia, X.-H.; Chen, H.-Y. Energy level engineering of MoS_2 by transition-metal doping for accelerating hydrogen evolution reaction. *J. Am. Chem. Soc.* **2017**, *139*, 15479−15485.
(52) Wang, Q.; Zhao, Z. L.; Dong, S.; He, D.; Lawrence, M. J.; Han, S.; Cai, C.; Xiang, S.; Rodriguez, P.; Xiang, B.; et al. Design of active nickel single-atom decorated MoS_2 as a pH-universal catalyst for hydrogen evolution reaction. *Nano Energy* **2018**, *53*, 458−467.

https://doi.org/10.1021/acscatal.2c00759
ACS Catal. 2022, 12, 7687−7695